AGU PUBLICATIONS

JGR

Journal of Geophysical Research: Space Physics

RESEARCH ARTICLE
10.1002/2015JA021822

Key Points:
- A new type of ion spectral structure —"trunk-like"—is reported
- The trunk structures are present in He^+ and O^+ ions but not in H^+
- Simulations are performed to gain insight into the trunk formation mechanism

Correspondence to:
J.-C. Zhang,
Jichun.Zhang@unh.edu

Citation:
Zhang, J.-C., et al. (2015), "Trunk-like" heavy ion structures observed by the Van Allen Probes, *J. Geophys. Res. Space Physics*, *120*, 8738–8748, doi:10.1002/2015JA021822.

Received 18 AUG 2015
Accepted 2 OCT 2015
Accepted article online 5 OCT 2015
Published online 27 OCT 2015

"Trunk-like" heavy ion structures observed by the Van Allen Probes

J.-C. Zhang[1], L. M. Kistler[1], H. E. Spence[1], R. A. Wolf[2], G. Reeves[3], R. Skoug[3], H. Funsten[3], B. A. Larsen[3], J. T. Niehof[1], E. A. MacDonald[4], R. Friedel[3], C. P. Ferradas[1], and H. Luo[5]

[1]Space Science Center, University of New Hampshire, Durham, New Hampshire, USA, [2]Department of Physics and Astronomy, Rice University, Houston, Texas, USA, [3]ISR Space Science and Applications, Los Alamos National Laboratory, Los Alamos, New Mexico, USA, [4]Geospace Physics Laboratory, NASA/GSFC, Greenbelt, Maryland, USA, [5]Institute of Geology and Geophysics, Chinese Academy of Sciences, Beijing, China

Abstract Dynamic ion spectral features in the inner magnetosphere are the observational signatures of ion acceleration, transport, and loss in the global magnetosphere. We report "trunk-like" ion structures observed by the Van Allen Probes on 2 November 2012. This new type of ion structure looks like an elephant's trunk on an energy-time spectrogram, with the energy of the peak flux decreasing Earthward. The trunks are present in He^+ and O^+ ions but not in H^+. During the event, ion energies in the He^+ trunk, located at $L = 3.6–2.6$, magnetic local time (MLT) = 9.1–10.5, and magnetic latitude (MLAT) = −2.4–0.09°, vary monotonically from 3.5 to 0.04 keV. The values at the two end points of the O^+ trunk are energy = 4.5–0.7 keV, $L = 3.6–2.5$, MLT = 9.1–10.7, and MLAT = −2.4–0.4°. Results from backward ion drift path tracings indicate that the trunks are likely due to (1) a gap in the nightside ion source or (2) greatly enhanced impulsive electric fields associated with elevated geomagnetic activity. Different ion loss lifetimes cause the trunks to differ among ion species.

1. Introduction

Particles that originate in the solar wind or ionosphere are injected from the plasma sheet freshly into the inner magnetosphere during magnetic storms and substorms. The injection of the particles into the inner magnetosphere results in a toroid-shaped ring current at radial distances of ~2–7 R_E. The current is carried primarily by ~1–200 keV ions (mainly H^+, O^+, and He^+) and electrons, which azimuthally drift around the Earth [*Gonzalez et al.*, 1994; *Daglis et al.*, 1999]. Particles in the ring current are lost via dayside flow out the magnetopause, as well as by charge exchange, Coulomb collisions, and wave-particle interactions [e.g., *Kistler et al.*, 1989; *Fok et al.*, 1991; *Jordanova et al.*, 1996; *Kozyra et al.*, 1998; *Liemohn et al.*, 1999, 2001].

The inner magnetosphere is a highly dynamic region where multiple populations, including the cold plasmasphere, energetic ring current, and relativistic radiation belt particles, overlap and interact with each other. The dynamics of these particle populations are controlled by the time-varying magnetic and electric fields in this region. Conversely, the particle populations also generate currents that affect both the magnetic field and the electric field [*Gonzalez et al.*, 1994; *Daglis et al.*, 1999].

Several spacecraft missions have detected various ion spectral features in the inner magnetosphere. These include "nose-like" structures [e.g., *Smith and Hoffman*, 1974; *Ejiri et al.*, 1980; *Shirai et al.*, 1997; *Fennell et al.*, 1998; *Peterson et al.*, 1998; *Li et al.*, 2000; *Ganushkina et al.*, 2001; *Buzulukova et al.*, 2003; *Ebihara et al.*, 2004; *Vallat et al.*, 2007], "wedge-like" dispersions [e.g., *Ebihara et al.*, 2001; *Yamauchi et al.*, 2006], ion gaps [e.g., *Kovrazhkin et al.*, 1999], and stagnation dips [e.g., *Lennartsson et al.*, 1979]. These ion structures are named after the characteristic shapes of energy bands or gaps in the energy-time spectrograms of in situ measured ion fluxes. They constitute the observational signatures of ion acceleration, transport, and loss in the global magnetosphere. The ion structures are attributed to the single or combined effect of several factors governing ion access to the inner magnetosphere: convection, corotation, magnetic gradient and curvature drifts, ion losses, and changes in the convection electric field and/or the ion source population. In the inner magnetosphere, keV ions are characterized by more complex spectral structures than electrons. The main reason is that the directions of the corotation and magnetic gradient/curvature drift are opposite for ions but the same for electrons. Near the inner boundary of the plasma sheet where the corotation electric field becomes more important than the large-scale dawn-to-dusk convection electric field, a net ion drift direction can be either eastward or westward, but electrons normally drift eastward.

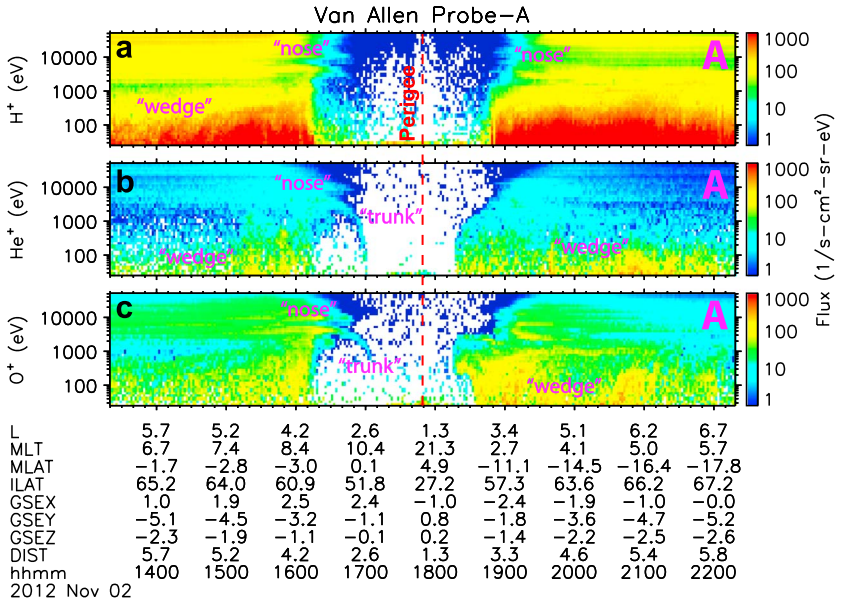

Figure 1. RBSP-ECT HOPE H^+, He^+, and O^+ spectrograms on the Van Allen Probe-A during an entire orbit, centered at perigee, on 2 November 2012. At the bottom is the ephemeris information of the Van Allen Probe: *L* (= L_TS04), magnetic local time (MLT, hours), magnetic latitude (MLAT, degrees), invariant latitude (ILAT, degrees), *X*, *Y*, and *Z* (R_E) in the GSE coordinate system, distance from the center of the Earth (DIST, R_E), and universal time (UT, hours). (a–c) The vertical red dashed line denotes the time of the perigee.

In this study, we report a new type of ion structure observed by the Helium, Oxygen, Proton, and Electron (HOPE) mass spectrometer in the Radiation Belt Storm Probes - Energetic Particle Composition and Thermal Plasma (RBSP-ECT) suite on board the Van Allen Probes. The spectral feature of the new ion structures is similar to an elephant's nose, i.e., "trunk-like". This paper is organized as follows: after section 1 (current section), we describe the instrumentation of the Van Allen Probes in section 2. Section 3 presents the observations of the trunk-like ion structures, solar wind and geomagnetic conditions, and trunk simulations. Discussion and conclusions from the work follow in section 4.

2. Instrumentation

The Van Allen Probes mission, formerly known as the Radiation Belt Storm Probes (RBSP) mission [*Kessel et al.*, 2013; *Mauk et al.*, 2013], consists of two spacecraft in almost the same highly elliptical, low-inclination (10°) orbit with a perigee of 1.1 Earth radii (R_E), an apogee of 5.8 R_E, and a period of ~9 h. The perigee-apogee line, i.e., the line of apsides, precesses in local time at a rate of ~210° per year. The orbits of the two probes are slightly different, and one probe laps the other every ~2.5 months. As a result, the interspacecraft distance periodically varies between ~0.1 to ~5 R_E and resampling times for a specific region change from minutes to 4.5 h. A comprehensive suite of instruments, identical on the two Van Allen Probes (−A and −B), measures a variety of parameters in particles (electrons, ions, and ion composition), magnetic field (**B**), electric field (**E**), and waves (**δE** and **δB**).

HOPE [*Funsten et al.*, 2013] is the low-energy instrument of the RBSP-ECT instrument suite [*Spence et al.*, 2013]. Using an electrostatic top-hat analyzer and the time-of-flight technology, the HOPE mass spectrometer measures electrons and ions in the energy range of ~1 eV–52 keV and distinguishes composition of three major ion species, H^+, He^+, and O^+. The measurement methodology and design of the HOPE instrument are intended for the reduction of the intense radiation background induced by relativistic particles and for valid plasma measurements in the harsh environment of the Earth's radiation belts.

3. Observations and Simulations

3.1. Trunk-Like Ion Structures

Figure 1 shows H^+, He^+, and O^+ energy-time flux spectrograms from HOPE on the Van Allen Probe-A for a full 9 h orbit from 1320 to 2220 UT on 2 November 2012. HOPE data presented here are spin averaged from

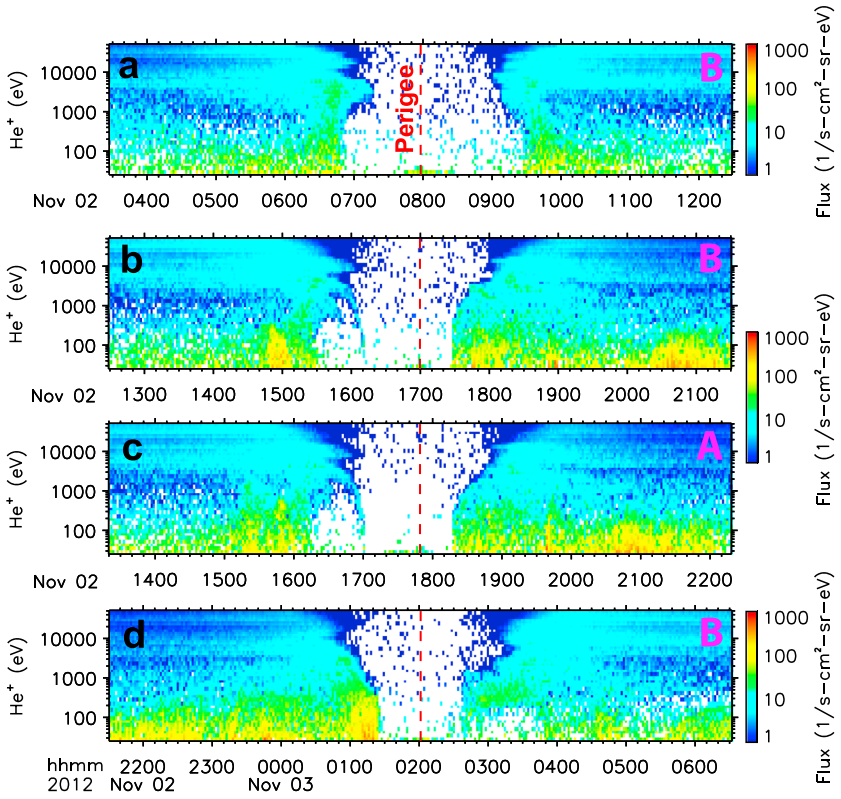

Figure 2. Similar format to Figure 1 but only for HOPE He^+ spectrograms on (a, b, and d) three consecutive orbits of the Van Allen Probe-B and (a) one orbit of the Van Allen Probe-A. Figure 2c is identical to Figure 1b.

Release 2 of the ECT data set. For the purpose of comparison, the fluxes of different ion species are plotted in the same range. Several ephemeris parameters of the spacecraft are included at the bottom of the figure. The *L* value (=L_TS04) is computed with the Tsyganenko and Sitnov empirical magnetic field model (TS04) [*Tsyganenko and Sitnov*, 2005]. While the inclination of the spacecraft orbit is fixed at 10°, its magnetic latitude (MLAT) can vary in the range of −21° to 21° due to the tilt of the geomagnetic axis and the precession of the line of apsides [*Mauk et al.*, 2013]. The plotting period is centered at perigee and extends for an entire orbit, i.e., 8.98 h. The perigee, marked by the vertical red dashed line, is at the time when the radial distance (DIST) is the minimum.

While nose-like and wedge-like spectral features are present in the spectrogram plots of all the three ion species, trunk-like structures are clearly displayed only in those of heavy He^+ and O^+ ions on the inbound perigee pass. HOPE electron spectra (not shown) do not exhibit trunk features. The He^+ trunk (Figure 1b) extends to a much lower energy than the O^+ trunk (Figure 1c), i.e., to 43 eV in He^+ compared to 723 eV in O^+. At higher and lower energy compared to the base of the trunks, nose-like spectral features are present; the lower energy feature is more like a secondary trunk (also see Figure 2b). These trunk structures differ from the well-known nose structures. Noses are observed at a single energy across a range of *L*; the energy of the peak flux within a trunk shows a strong dependence on *L*. Table 1 lists several properties of the main He^+

Table 1. Properties of the Heavy Ion Trunk Structures

UT	He^+ *E* (keV)	O^+ *E* (keV)	*L*	MLT	MLAT (°)
1627:20	3.5	4.5	3.6	9.1	−2.4
1653:20	1	2.5	2.8	10.0	−0.7
1659:00	0.1	1.8	2.7	10.4	−0.04
1700:40	0.04	1.5	2.6	10.5	0.09
1703:40	-	0.7	2.5	10.7	0.4

trunk and the O^+ trunk as shown in Figures 1b and 1c. The six columns show the values of UT, He^+ energy, O^+ energy, *L*, magnetic local time (MLT), and magnetic latitude (MLAT) at several sample points along the central line of the trunk structures, respectively. The first and fourth rows indicate the values at the two end points of the He^+ trunk (Figure 1b): energy = 3.5–0.04 keV, *L* = 3.6–2.6, MLT = 9.1–10.5, and MLAT = −2.4–0.09°. The values at the two end points of the O^+ trunk (Figure 1c) shown in the first and fifth rows are energy = 4.5–0.7 keV, *L* = 3.6–2.5, MLT = 9.1–10.7, and MLAT = −2.4–0.4°.

No trunk-like structure exists on the outbound perigee pass. The inner edge of lower *L* shell access in each species, i.e., the lowest penetration boundary of convecting ions, is deeper than that on the inbound pass. The difference in the lowest injection *L* value between the inbound and outbound passes is 0.6 (0.8) for H^+ (He^+ and O^+). This is due to the dependence of the location of the inner injection boundary on MLT [*Ejiri et al.*, 1980].

Figure 2 illustrates He^+ spectral features observed by the HOPE instrument on three consecutive orbits of the Van Allen Probe-B (a, b, and d) and one orbit of the Van Allen Probe-A (c). Figure 2c is the same as Figure 1b. He^+ spectrograms before and after the trunk orbit of the Van Allen Probe-A (Figure 2c) are not shown because they are almost identical to their counterparts on the Van Allen Probe-B (Figures 2a and 2d). The spectrograms of He^+, as well as those of H^+ and O^+ (not shown), from the two spacecraft in the same orbit with a temporal separation of 50 min are comparable. The trunk on the Van Allen Probe-A has a slightly wider spatial extent than that on the Van Allen Probe-B. Trunk structures were not detected on the inbound passes of the orbits right before and after the trunk orbit (Figures 2a and 2d). As for the outbound passes of the four orbits (Figures 2a–2d), no trunk is present at all, but in Figure 2d a broad energy band appears on the outbound pass over the energy range of the trunk and extends to a low *L* shell, where *L* = 2.3, MLT = 1.0, and MLAT = 9.8°.

3.2. Solar Wind and Geomagnetic Conditions

Figure 3 shows 1 min solar wind plasma number density *N*, bulk flow speed *V*, dynamic pressure P_{dyn}, IMF B_y and B_z in the GSM coordinates, polar cap potential drop (PCP), *Kp*, and the *Sym-H* index during the moderate storm occurring from 31 October to 3 November 2012. The high-resolution solar wind measurements are from the online OMNIWeb Plus data set [*Papitashvili and King*, 2006]. There is an ~8 h gap in the solar wind data close to the end of the plotting period. PCP, a proxy for the convection electric field intensity, is given by $PCP = 57.6 P_{dyn}{}^{1/3} E/(P_{dyn}{}^{1/2} + 0.43E) + 10^{-4} V^2$, where PCP is in kV, P_{dyn} in nPa, solar wind electric field *E* in mV/m, and *V* in km/s. $E = 0$ for northward IMF and $V|B_z|$ for southward. The first term in the PCP formula is given by *Siscoe et al.* [2002], and the second is a viscous term from *Boyle et al.* [1997]. The solar wind and PCP data are shifted backward by 10 min to align the solar wind shock with the storm sudden commencement (SSC) at 1540 UT, 31 October 2012. The 10 min time shift is within expected aberrations when solar wind data are propagated from a satellite (e.g., around the first Lagrange point L1) to the Earth for the creation of the OMNIWeb database [*Weimer et al.*, 2003; *Weimer and King*, 2008]. The first vertical red dashed line marks the arrival time of the solar wind shock. The two vertical magenta dash-dotted (dotted) lines indicate the time period of the trunk observed by the Van Allen Probe-B (A), i.e., 1537:20–1612:20 (1627:20–1700:40) UT, 2 November 2012. In Figures 3d and 3g, the horizontal black dashed line marks the zero value.

The moderate storm, during which minimum *Sym-H* is equal to −68 nT at 2001 UT on 1 November 2012, was driven by a magnetic cloud (MC) with an extended sheath region [*Burlaga et al.*, 1981; *Zhang et al.*, 2004]. The three vertical red dashed lines in Figure 3 denote both of the sheath and MC regions. Further solar wind disturbances behind the MC event may be due to the eroded MC flux rope, which results from magnetic reconnection at the boundary between the sheath and MC [*Ruffenach et al.*, 2012]. The trunks occurred in the middle recovery phase of the geomagnetic storm.

3.3. Backward Ion Drift Path Tracings

Figure 4 demonstrates total drift time results from the backward tracings of ion drift trajectories from given probe positions for 50 h or until the ions reach the assumed tailward injection boundary at *L* = 10. Tracing results under different conditions (see below) are presented. The particle tracing technique has been previously utilized [e.g., *Buzulukova et al.*, 2002; *Ebihara et al.*, 2008]. The tracing simulations are performed with the Weimer96 convection electric field [*Weimer*, 1996], a corotational electric field, and a dipole magnetic field. Charge exchange is assumed to be the only ion loss process along the drift paths. For the charge

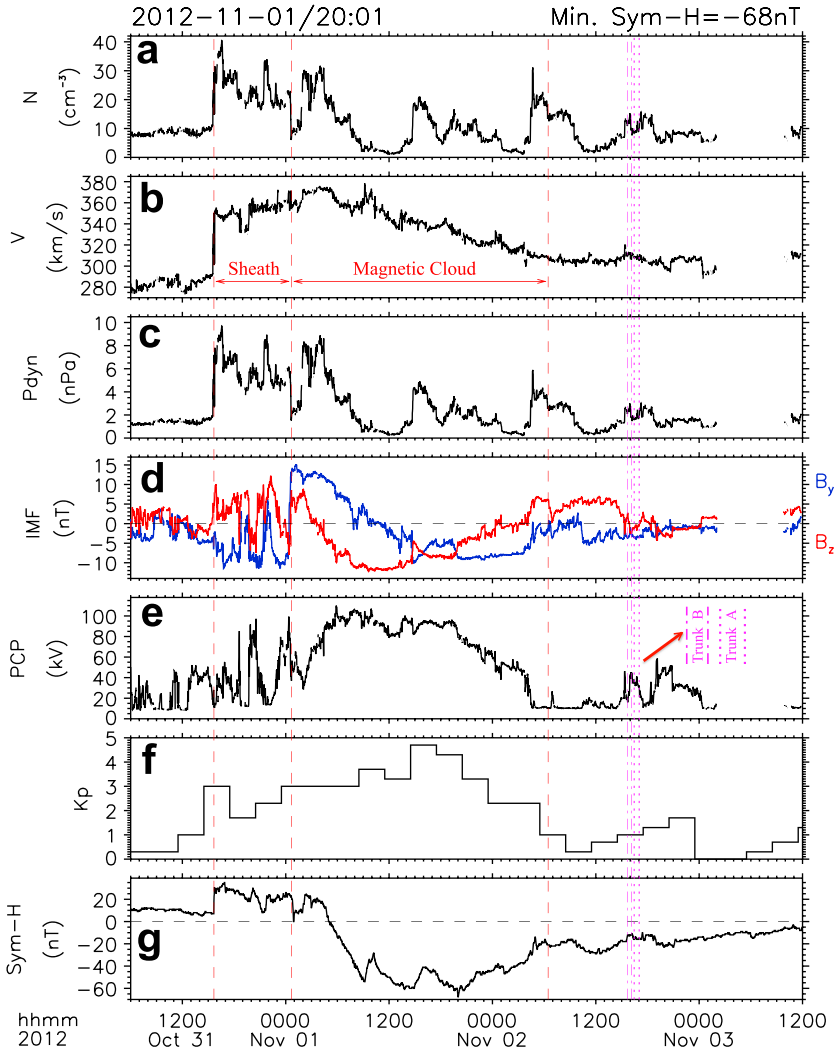

Figure 3. Solar wind plasma and interplanetary magnetic field (IMF) parameters, polar cap potential drop (PCP), *Kp*, and *Sym-H* from 0600 UT, 31 October to 1200 UT, 3 November 2012.

exchange loss calculations, equatorial neutral hydrogen number density is inferred from a model derived by *Hodges* [1994] and charge exchange cross sections are given by *Smith and Bewtra* [1978a].

Figures 4a and 4b show the drift time from $L = 10$ to the observation location with the specified time-dependent electric fields using the standard Weimer96 settings. Only the color bars are different between the nominal tracing results (Figures 4a and 4b). This is to emphasize the difference in the drift time in the isolated low-energy region, the "island", in Figure 4b. If a trajectory never reaches $L = 10$ in the 50 tracing hours, meaning that either the drift path is closed or the particle drifts very slowly, then white is shown. As can be seen, with a steady tail source, an island structure is formed and has an outer boundary featuring a trunk-like shape at the lower L end. Therefore, one way that the trunk could be formed (Case #1) is with a time-dependent variation in the source, where the injection of ions in the island with shorter drift time (≤34.0 h) than trunk ions is halted. The resulting drift time spectrum, computed assuming no source population if the total drift time is in the range of 29.2–34.0 h, is shown in Figure 4c. The choice of the temporal gap in the source is roughly determined by the realism of the observed trunk spectral features shown in Figure 1b, especially the trunk thickness. This threshold would depend on the specifics of a particular event.

The disappearance of the ions in the island spans ~5 h in UT. It would rotate eastward (see the green line in Figure 6a) and form a cold ion gap along the drift path, i.e., for several hours in MLT. This localized structure might be the reason that the trunk was not detected by the Van Allen Probe-B at the same MLT location

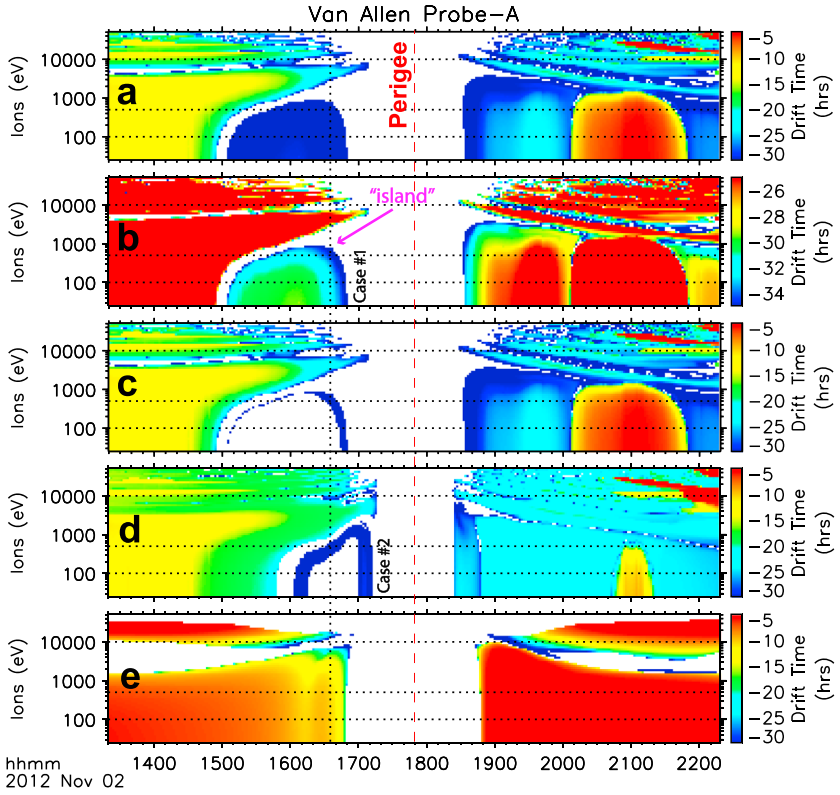

Figure 4. Calculated total ion backward drift time (negative) from the positions of the Van Allen Probe-A to the assumed ion source at $L = 10$ under different conditions: nominal tracing results with the color scale adjusted for (a and b) two levels, (c) assuming an ion source gap, (d) under made-up extreme solar wind conditions (d), and (e) using constant model inputs. The plotting time period is the same as that in Figure 1. The vertical red dashed line denotes the time of the perigee, the vertical black dotted line indicates the time of 1635 UT, and the horizontal dotted lines mark the energy values of 0.1, 0.5, and 10 keV.

during the next orbit (Figure 2d), and there was a disappearance of cold ions ($<$ ~200 eV) on the outbound pass of the Van Allen Probe-B at ~2 MLT from 0240–0350 UT on 3 November 2012 (Figure 2d).

The effect of a second mechanism to form the trunk (Case #2) is shown in Figure 4d. In this case, a modified solar wind condition (i.e., Weimer96 input IMF B_z is subtracted by 40 nT from 0900 to 2200 UT on 1 November 2012) is simulated. Surprisingly, particle tracing within these fields directly yields a trunk (the low L side of the arch structure) in the accessibility to particles from the presumed $L = 10$ injection region. The peak value and duration of the made-up southward IMF B_z are too "extreme" to exist in reality. This tracing run is for the purpose of experiment. Still, the modification to IMF B_z aims to create a cumulative effect on ion drift of greatly enhanced impulsive electric fields associated with elevated geomagnetic activity, which are lacking in the empirical Weimer96 model. A set of peak values and durations of IMF B_z have been tested. It turns out that a "decent" arch structure (Figure 4d) can be created with the input modification above.

Note that the observed He^+ trunk (Figure 1b) and the simulated trunks (Figures 4c and 4d) differ in several aspects, e.g., in ion energy and occurrence UT. The separate island, which is formed in the simulations with the standard Weimer96 (Figure 4b), is not evident in the observations. The reason for the island, and why it might not be observed in this case, is discussed below. The observations show that the trunk feature connects smoothly to structures in the ion spectra. For example, in Figures 1b and 1c, there is a peak in the H^+ and O^+ (clearer) fluxes at around 4 keV near 1600 UT, which is blended with the observed trunk feature. However, the simulated trunks are not connected to other spectral structures at all; this simulation result yet implies that the trunk ion populations are different from the nontrunk populations (difficult to be identified in the observations, though). The data-model discrepancies may be due to the fact that the empirical Weimer96 electric field model, combined with the simple dipole magnetic field model, cannot accurately

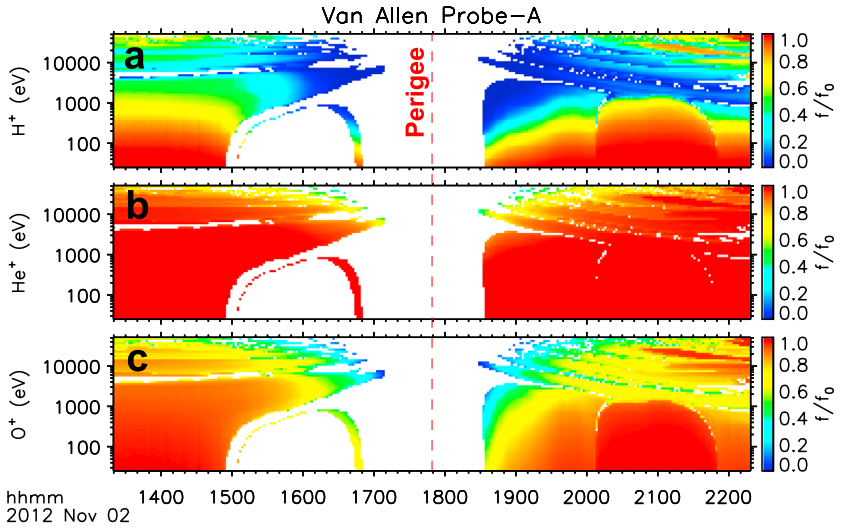

Figure 5. Calculated ratios of H^+ (a), He^+ (b), and O^+ (c) fluxes at the locations of the Van Allen Probe-A and in the assumed ion source at $L = 10$. The plotting time period is the same as Figure 1. The vertical red dashed line denotes the time of the perigee.

reproduce particular ion spectral features but can still indicate the trends. While being able to fairly well reproduce the large-scale dawn-to-dusk convection electric field, Weimer96 does not include impulsive, localized electric fields associated with substorm injections [e.g., *Zhang et al.*, 2008, 2009]. The small-scale electric fields can cause diffusion, which may be effective enough to make the spectral structures blur into each other [*Gkioulidou et al.*, 2014; *Yang et al.*, 2014]. In addition, we only consider the ion source region from the outer boundary (assumed at $L = 10$) and do not include any other ion source or pre-existing particles in the trunk region. This can also result in much simpler or more idealized spectral features in the simulation results than those in the observations.

Wedges are not reproduced at all, because no variation is applied to the distribution function of the tailward ion source [*Ebihara et al.*, 2001]. Noses are reasonably well reproduced with Weimer96 and the dipole magnetic field. The fine spectral features in noses, i.e., multiple horizontal gaps in the higher-energy ions, are associated with the variations in solar wind (see Figure 3). Another run with constant inputs to Weimer96 is performed to evaluate the effects of the solar wind variations. The model inputs include Earth's dipole tilt angle, solar wind N and V, and IMF B_y and B_z [*Weimer*, 1996]. The fixed input values are those at 0600 UT, 31 October 2012, i.e., the plot start time of Figure 3. As shown in Figure 4e, when inputs to Weimer96 are fixed, only one main nose is present. The nose is basically formed with more deeply injected ions when the magnitudes of their $\mathbf{E}\times\mathbf{B}$ drift and magnetic gradient/curvature drift are comparable. The "canceled" net ion drift (due to the opposite directions of the two types of drifts) allows those ions to move more inward instead of around the Earth in either the eastward or westward direction. The variations in the solar wind parameters, affecting ion drift magnitudes, change the energy of those nose ions and thus result in the multiple spectral bands in the nose energy range [*Buzulukova and Vovchenko*, 2008].

Figure 5 shows the fraction of the initial flux remaining (f/f_0) after charge exchange losses along the drift path for the species H^+, He^+, and O^+, computed with the same halted ion source as in Figure 4c. Because the charge exchange loss rates depend on the ion species and energy, and how deeply the trajectory penetrates in L value [*Smith and Bewtra*, 1978b], these losses can create spectral gaps and features that appear differently for different species. There are clearly different depletion levels among H^+, He^+, and O^+. The differences are more distinct at lower L shells and in higher energies. Since H^+ has the shortest charge exchange lifetime, H^+ f/f_0 in the upper energy trunk is almost 0, while He^+ is barely depleted. Thus, the species dependence observed is consistent with the model that the trunk is caused by ions on drift paths with long drift time. The pitch angle distribution of trunk ions is centered around 90° (not shown), which is also consistent with the effect of charge exchange on drifting particles, i.e., becoming more anisotropic over time [*Goldstein et al.*, 2012]. Coulomb collisions with cold plasma in the plasmasphere [*Fok et al.*, 1991] are perhaps the other loss process that could further deplete ions and even wipe out H^+ and O^+ in the lower energy trunk as shown

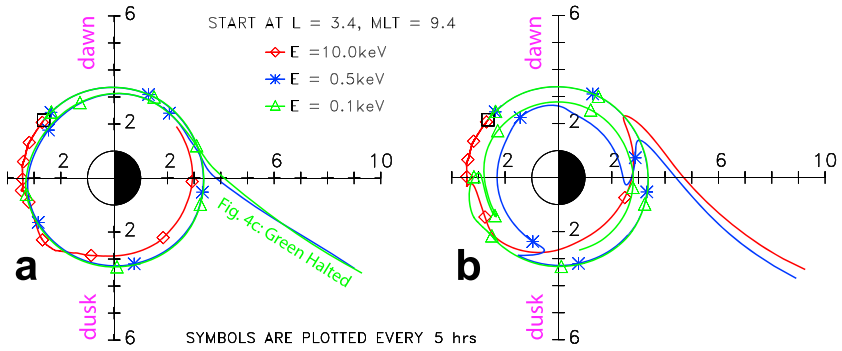

Figure 6. Fifty hour backward tracing of drift paths for singly charged ions (PA = 90°) at 1635 UT, 2 November 2012, corresponding to the cases indicated in Figures 4b (a, left) and 4d (b, right). All backward drifting ions start from the position of the Van Allen Probe-A at the time point, i.e., from $L = 3.4$ and MLT = 9.4. The solid tracing trajectories are plotted every 30 s unless they reach the model boundaries at $L = 10$. The symbols, i.e., red squares, blue stars, or green triangles, are plotted every 5 h until $L = 10$.

in Figure 1. For the trunk energy range, H^+ still has the shortest Coulomb collision lifetime among the three ion species [*Fok et al.*, 1991].

Figure 6 shows 50 h backward tracing of drift paths for three singly charged ions with energies of 0.1, 0.5, and 10 keV (see the horizontal dotted lines in Figure 4) at 1635 UT for the cases indicated in Figure 4b (left: Case #1), the Weimer96 electric field, and Figure 4d (right: Case #2), the extreme electric field. The 0.5 keV ion trajectory corresponds to the trunk. The ion trajectories last for either 50 hrs or end at $L \sim 10$ when the ions reach the boundary. The 10.0 keV ion drifts very slowly on a closed drift path in Case #1, but it is on an open drift path and has access to the tailward ion source in Case #2. Before reaching $L = 10$, the 0.5 keV trunk ion drifts an extra circle around the Earth in both cases. The 0.1 keV ion has a similar trajectory to the 0.5 keV ion in Case #1, but it is trapped on a closed drift trajectory in Case #2. More ion tracings indicate that all the trunk ions are from a source region with a narrow MLT range. For example, the ion source at $L = 10$ for the trunk ions in Figure 4c is in the MLT range of 21.6–22.8. In addition, in Case #1, a majority of the trunk ions have a total drift time just over 34.0 h. They were injected at $L = 10$ at ~0600 UT on 1 November 2012, which is in the middle of the storm main phase. If the injection of those ions under the trunk arch which have total drift time from 29.2 to 34.0 h and MLT at $L = 10$ from 22.2 to 22.9 (e.g., the green line in Figure 6a) is halted, a trunk would be formed from Figure 4b, as shown in Figure 4c. It is not expected to suspend the ion source for almost 5 h in UT during the main phase of the moderate storm. However, the source suspension is required only in low energies (i.e., <~800 eV in the trunk region), and the total drift time of the suspended ions seems to dominate a shorter time range (i.e., ~30–31 h), as shown in Figure 4b. In reality, the temporal gap of the ion source could be much narrower. The cause of the source gap might be associated with a variation in the cold ion source [e.g., *Ebihara et al.*, 2001] or the activity of a "depleted channel" or "plasma bubble" during the storm, which is characteristic of Earthward-traveling low-entropy flux tubes [e.g., *Sergeev and Lennartsson*, 1988; *Zhang et al.*, 2008, 2009].

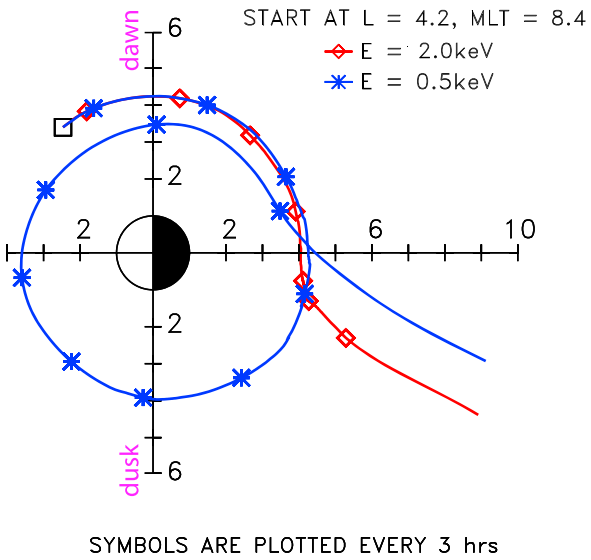

Figure 7. Similar to Figure 6a but for 0.5 and 2.0 keV singly charged ions at 1600 UT, 2 November 2012, starting from $L = 4.2$ and MLT = 8.4. The trajectory symbols are plotted every 3 h until $L = 10$.

Another figure, Figure 7, is intended to highlight the drift path differences between ions

inside and outside the island (Figures 4a and 4b). The particle tracing setup for Figure 7 is the same as Figure 6a but for 0.5 and 2.0 keV singly charged ions at 1600 UT, 2 November 2012. The backward-traced ions start from the spacecraft location at the time, i.e., from $L = 4.2$ and MLT = 8.4. At the time point, the particle energies are just below and above the spectral gap that separates the island from its surrounding spectral features. Consistent with the results in Figure 6a, the island ion (0.5 keV) drifts around the Earth almost a full circle more than the nonisland ion (2.0 keV). The spectral gap (Figures 4a and 4b) is thus caused by the distinct differences in the drift time and paths between the island and nonisland ions. Note that the 2.0 keV ion in Figure 7 drifts eastward but the 10.0 keV ion in Figure 6a goes westward. The reason is that their dominant drift component is different, i.e., $\mathbf{E} \times \mathbf{B}$ drift for the former but gradient-curvature drift for the latter.

4. Discussion and Conclusions

We report a new type of ion spectral feature in the inner magnetosphere—trunk-like ion structure. The trunk structures, observed in situ by the RBSP-ECT HOPE instrument on board the two Van Allen Probes on 2 November 2012, are present in the spectrograms of He^+ and O^+ ions but not in those of H^+. For the particular event, ion energies in the He^+ trunk, which is located at $L = 3.6–2.6$, MLT = 9.1–10.5, and MLAT = −2.4–0.09°, vary monotonically from 3.5 to 0.04 keV. The values at the two end points of the O^+ trunk are energy = 4.5–0.7 keV, $L = 3.6–2.5$, MLT = 9.1–10.7, and MLAT = −2.4–0.4°. Possible reasons that the trunk has been observed by the Van Allen Probes and not by earlier space missions, such as Cluster and THEMIS, include (1) more frequent crossings of the inner edge of the plasma sheet and (2) higher-fidelity measurements of plasma sheet ion fluxes and composition by the HOPE instrument in the harsh radiation belt environment.

The trunk-like structures are different from previously reported nose-like and wedge-like ion structures and require a new formation mechanism. Noses are characterized by narrow bands in energy, which extend down to low L shells but are nearly constant in energy [e.g., *Smith and Hoffman*, 1974; *Ejiri*, 1978]. They are normally due to the deeper injection of ions with a specific energy when the westward and eastward components of the $\mathbf{E} \times \mathbf{B}$ and gradient-curvature drifts of the ions become comparable in magnitude. *Ebihara et al.* [2001] suggested that a wedge-like structure, containing sub-keV ions, should result from the energy-dependent Earthward drift of ions in the plasma sheet when the distribution function of the ion source changes in time and space. The ion source variation can be related to a substorm injection and/or an ion flow channel in the tail. Although the outer layer of a wedge [e.g., *Ebihara et al.*, 2001; *Yamauchi et al.*, 2006; *Ebihara et al.*, 2008] looks similar to a trunk structure, the change of the structure thickness in energy and L is opposite between a trunk and a wedge: the higher the ion energy or the L, the wider the trunk but the thinner the wedge. The time scale of an observed wedge is also much smaller than a trunk, typically ~10 versus ~30 min on the Van Allen Probes. While noses and wedges often display multiple ion energy bands, the trunks we have reported only exist as a single, narrow structure on the inner ion penetration boundary. Another distinct difference between trunks and other ion structures is in occurrence frequency. Noses and wedges (predominantly on the dayside [*Ebihara et al.*, 2001]) occur frequently close to the inner edge of the plasma sheet. However, the trunks apparently occur only rarely. Visual inspection of HOPE ion spectra for ~2 months, i.e., 26 October 2012–31 December 2012, reveals only two more well-structured trunk structures in both He^+ and O^+ on each probe on 4 and 14 November, respectively. The two clear trunk events were also observed in the morning sector with an MLT range of ~8–10. Moreover, they occurred in the recovery phase of a magnetic storm as well. The former occurred in the late recovery phase of the 1 November 2012 moderate storm, and the latter was present in the middle recover phase of an intense storm (minimum $Sym\text{-}H = -117$ nT at 0725 UT on 14 November 2012). Collecting and examining more trunks to obtain their occurrence frequency, location, and conditions will be a topic for future work.

To gain insight into how trunks are formed, we perform backward tracings of ion drift paths from one-whole-orbit probe positions to the ion source region ($L = 10$) while considering the effect of the charge exchange loss. While there are several puzzling features in the trunks, the most significant one is their relative spectral narrowness. Our tracing results show that the source location for the trunk ions is small and the particles are initially injected over a short time. These most likely account for the narrowness of the trunk feature. The trunk ions are also found to have prolonged total drift time from $L = 10$ to the observation location, circling the Earth an extra time before reaching the observation points. The drift time is long enough to allow charge

exchange and Coulomb collisions to take effect and cause the trunk feature differences among ion species due to their different loss lifetimes. In particular, because H^+ has the shortest lifetime, it is completely depleted by the time it arrives at the region where a trunk would form. As a result, the trunks are present only in heavy ions. It is indicated that a trunk can be formed in two possible ways: (1) a gap in the nightside ion source or (2) greatly enhanced impulsive electric fields associated with elevated geomagnetic activity. Similar variation in the distribution function of the ion source has been used to explain the spectral gaps between wedges [*Ebihara et al.*, 2001]. However, an experimental run with the made-up solar wind condition implies that a trunk may also be formed from large impulsive electric fields that are often present during substorms/storms [*Zhang et al.*, 2008, 2009]. Further investigation is required to evaluate the relative importance of the two different mechanisms for the formation of a trunk.

Acknowledgments

This work was supported by RBSP-ECT funding provided by JHU/APL contract 967399 under NASA's Prime Contract No. NAS5-01072. Work at UNH was also supported by NASA under grant NNX13AE23G. Work at LANL was performed under the auspices of the United States Department of Energy. HOPE data used in this paper were downloaded from the Van Allen Probes ECT website at http://www.rbsp-ect.lanl.gov/rbsp_ect.php. Solar wind plasma/IMF data and the *Kp* and *Sym-H* indices were obtained from the GSFC/SPDF OMNIWeb interface at http://omniweb.gsfc.nasa.gov. D.R. Weimer provided the Weimer96 model for the ion tracings. J.-C. Zhang thanks Richard Thorne, Mike Liemohn, and Noé Lugaz for their helpful discussions.

References

Boyle, C. B., P. H. Reiff, and M. R. Hairston (1997), Empirical polar cap potentials, *J. Geophys. Res.*, *102*(A1), 111–125, doi:10.1029/96JA01742.

Burlaga, L., E. Sittler, F. Mariani, and R. Schwenn (1981), Magnetic loop behind an inter-planetary shock: Voyager, Helios, and Imp 8 observations, *J. Geophys. Res.*, *86*(A8), 6673–6684, doi:10.1029/JA086iA08p06673.

Buzulukova, N., and V. Vovchenko (2008), Modeling of proton nose structures in the inner magnetosphere with a self-consistent electric field model, *J. Atmos. Sol. Terr. Phys.*, *70*, 2–4, doi:10.1016/j.jastp.2007.08.028.

Buzulukova, N. Y., R. A. Kovrazhkin, A. L. Glazunov, J. A. Sauvaud, N. Y. Ganushkina, and T. I. Pulkkinen (2003), Stationary nose structures of protons in the inner magnetosphere: Observations by the ION instrument onboard the Interball-2 satellite and modeling, *Cosmic Res. Engl. Trans.*, *41*, 1, doi:10.1023/A:1022343327565.

Buzulukova, N. Y., Y. I. Galperin, R. A. Kovrazhkin, A. L. Glazunov, G. A. Vladimirova, H. Stenuit, J. A. Sauvaud, and D. C. Delcourt (2002), Two types of ion spectral gaps in the quiet inner magnetosphere: Interball-2 observations and modeling, *Ann. Geophys.*, *20*, 3, doi:10.5194/angeo-20-349-2002.

Daglis, I. A., R. M. Thorne, W. Baumjohann, and S. Orsini (1999), The terrestrial ring current: Origin, formation, and decay, *Rev. Geophys.*, *37*(4), 407–438, doi:10.1029/1999RG900009.

Ebihara, Y., L. M. Kistler, and L. Eliasson (2008), Imaging cold ions in the plasma sheet from the Equator-S satellite, *Geophys. Res. Lett.*, *35*, L15103, doi:10.1029/2008GL034357.

Ebihara, Y., M. Yamauchi, H. Nilsson, R. Lundin, and M. Ejiri (2001), Wedge-like dispersion of sub-keV ions in the dayside magnetosphere: Particle simulation and Viking observation, *J. Geophys. Res.*, *106*(A12), 29,571–29,584, doi:10.1029/2000JA000227.

Ebihara, Y., M. Ejiri, H. Nilsson, I. Sandahl, M. Grande, J. F. Fennell, J. L. Roeder, D. R. Weimer, and T. A. Fritz (2004), Multiple discrete-energy ion features in the inner magnetosphere: 9 February 1998, event, *Ann. Geophys.*, *22*, 1297–1304, doi:10.5194/angeo-22-1297-2004.

Ejiri, M. (1978), Trajectory traces of charged-particles in the magnetosphere, *J. Geophys. Res.*, *83*(A10), 4798–4810, doi:10.1029/JA083iA10p04798.

Ejiri, M., R. A. Hoffman, and P. H. Smith (1980), Energetic particle penetrations into the inner magnetosphere, *J. Geophys. Res.*, *85*(A2), 653–663, doi:10.1029/JA085iA02p00653.

Fennell, J. F., et al. (1998), Multiple discrete-energy ion features in the inner magnetosphere: Polar observations, in *Physics of Space Plasmas*, pp. 395, MIT Center for Theoretical Geo/Cosmo Plasma Physics, Cambridge, Mass.

Fok, M. C., J. U. Kozyra, A. F. Nagy, and T. E. Cravens (1991), Lifetime of ring current particles due to coulomb collisions in the plasmasphere, *J. Geophys. Res.*, *96*(A5), 7861–7867, doi:10.1029/90JA02620.

Funsten, H. O., et al. (2013), Helium, Oxygen, Proton, and Electron (HOPE) Mass spectrometer for the radiation belt storm probes mission, *Space Sci. Rev.*, doi:10.1007/s11214-013-9968-7.

Ganushkina, N. Y., T. I. Pulkkinen, V. F. Bashkirov, D. N. Baker, and X. L. Li (2001), Formation of intense nose structures, *Geophys. Res. Lett.*, *28*(3), 491–494, doi:10.1029/2000GL011955.

Gkioulidou, M., A. Y. Ukhorskiy, D. G. Mitchell, T. Sotirelis, B. H. Mauk, and L. J. Lanzerotti (2014), The role of small-scale ion injections in the buildup of Earth's ring current pressure: Van Allen Probes observations of the 17 March 2013 storm, *J. Geophys. Res. Space Physics*, *119*, 7327–7342, doi:10.1002/2014JA020096.

Goldstein, J., P. Valek, D. J. McComas, and J. Redfern (2012), TWINS energetic neutral atom observations of local-time-dependent ring current anisotropy, *J. Geophys. Res.*, *117*, A11213, doi:10.1029/2012JA017804.

Gonzalez, W. D., J. A. Joselyn, Y. Kamide, H. W. Kroehl, G. Rostoker, B. T. Tsurutani, and V. M. Vasyliunas (1994), What is a geomagnetic storm?, *J. Geophys. Res.*, *99*(A4), 5771–5792, doi:10.1029/93JA02867.

Hodges, R. R. (1994), Monte carlo simulation of the terrestrial hydrogen exosphere, *J. Geophys. Res.*, *99*(A12), 23,229–23,247, doi:10.1029/94JA02183.

Jordanova, V. K., L. M. Kistler, J. U. Kozyra, G. V. Khazanov, and A. F. Nagy (1996), Collisional losses of ring current ions, *J. Geophys. Res.*, *101*(A1), 111–126, doi:10.1029/95JA02000.

Kessel, R. L., N. J. Fox, and N. Weiss (2013), The Radiation Belt Storm Probes (RBSP) and Space Weather, *Space Sci. Rev.*, doi:10.1007/s11214-012-9953-6.

Kistler, L. M., F. M. Ipavich, D. C. Hamilton, G. Gloeckler, B. Wilken, G. Kremser, and W. Studemann (1989), Energy-spectra of the major ion species in the ring current during geomagnetic storms, *J. Geophys. Res.*, *94*(A4), 3579–3599, doi:10.1029/JA094iA04p03579.

Kovrazhkin, R. A., J. A. Sauvaud, and D. C. Delcourt (1999), INTERBALL-Auroral observations of 0.1–12 keV ion gaps in the diffuse auroral zone, *Ann. Geophys.*, *17*, 734–742, doi:10.1007/S005850050802.

Kozyra, J. U., M. C. Fok, E. R. Sanchez, D. S. Evans, D. C. Hamilton, and A. F. Nagy (1998), The role of precipitation losses in producing the rapid early recovery phase of the Great Magnetic Storm of February 1986, *J. Geophys. Res.*, *103*(A4), 6801–6814, doi:10.1029/97JA03330.

Lennartsson, W., E. G. Shelley, R. D. Sharp, R. G. Johnson, and H. Balsiger (1979), Some initial ISEE-1 results on the ring current composition and dynamics during the magnetic storm of December 11, 1977, *Geophys. Res. Lett.*, *6*(6), 483–486, doi:10.1029/GL006i006p00483.

Li, X. L., D. N. Baker, M. Temerin, W. K. Peterson, and J. F. Fennell (2000), Multiple discrete-energy ion features in the inner magnetosphere: Observations and simulations, *Geophys. Res. Lett.*, *27*(10), 1447–1450, doi:10.1029/1999GL010745.

Liemohn, M. W., J. U. Kozyra, C. R. Clauer, and A. J. Ridley (2001), Computational analysis of the near-Earth magnetospheric current system during two-phase decay storms, *J. Geophys. Res.*, *106*(A12), 29,531–29,542, doi:10.1029/2001JA000045.

Liemohn, M. W., J. U. Kozyra, V. K. Jordanova, G. V. Khazanov, M. F. Thomsen, and T. E. Cayton (1999), Analysis of early phase ring current recovery mechanisms during geomagnetic storms, *Geophys. Res. Lett.*, *26*(18), 2845–2848, doi:10.1029/1999GL900611.

Mauk, B. H., N. J. Fox, S. G. Kanekal, R. L. Kessel, D. G. Sibeck, and A. Ukhorskiy (2013), Science objectives and rationale for the Radiation Belt Storm Probes mission, *Space Sci. Rev.*, doi:10.1007/s11214-012-9908-y.

Papitashvili, N. E., and J. H. King (2006), A draft high resolution OMNI data set, *Eos Trans. AGU, Jt. Assem. Suppl., Abstract SM33A-02*, *87*, 36.

Peterson, W. K., K. J. Trattner, O. W. Lennartsson, H. L. Collin, T. I. Pulkkinen, P. K. Toivanen, J. F. Fennell, J. L. Roeder, D. N. Baker, and T. A. Fritz (1998), Imaging the plasma sheet with energetic ions from the Polar satellite, in *Proc. of ICS-4*, 813 pp., Terra Sci. Publ., Tokyo.

Ruffenach, A., et al. (2012), Multispacecraft observation of magnetic cloud erosion by magnetic reconnection during propagation, *J. Geophys. Res.*, *117*, A09101, doi:10.1029/2012JA017624.

Sergeev, V. A., and W. Lennartsson (1988), Plasma sheet at X ≈ −20 R_E during steady magnetospheric convection, *Planet. Space Sci.*, *36*, 4, doi:10.1016/0032-0633(88)90124-9.

Shirai, H., K. Maezawa, M. Fujimoto, T. Mukai, Y. Saito, and N. Kaya (1997), Monoenergetic ion drop-off in the inner magnetosphere, *J. Geophys. Res.*, *102*(A9), 19,873–19,881, doi:10.1029/97JA01150.

Siscoe, G. L., G. M. Erickson, B. U. O. Sonnerup, N. C. Maynard, J. A. Schoendorf, K. D. Siebert, D. R. Wiemer, W. White, and G. R. Wilson (2002), Hill model of transpolar potential saturation: Comparisons with MHD simulations, *J. Geophys. Res.*, *107*(A6), SMP 8-1–SMP 8-8, doi:10.1029/2001JA000109.

Smith, P. H., and N. K. Bewtra (1978a), Charge exchange lifetimes for ring current ions, *Space Sci. Rev.*, *22*, 301–318.

Smith, P. H., and N. K. Bewtra (1978b), Charge-exchange lifetimes for ring current ions, *Space Sci. Rev.*, *22*, 3.

Smith, P. H., and R. A. Hoffman (1974), Direct observations in the dusk hours of the characteristics of the storm time ring current particles during the beginning of magnetic storms, *J. Geophys. Res.*, *79*(7), 966–971, doi:10.1029/JA079i007p00966.

Spence, H. E., et al. (2013), Science goals and overview of the Radiation Belt Storm Probes (RBSP) Energetic Particle, Composition, and Thermal Plasma (ECT) suite on NASA's Van Allen Probes mission, *Space Sci. Rev.*, doi:10.1007/s11214-013-0007-5.

Tsyganenko, N. A., and M. I. Sitnov (2005), Modeling the dynamics of the inner magnetosphere during strong geomagnetic storms, *J. Geophys. Res.*, *110*, A03208, doi:10.1029/2004JA010798.

Vallat, C., N. Ganushkina, I. Dandouras, C. P. Escoubet, M. G. G. T. Taylor, H. Laakso, A. Masson, J. A. Sauvaud, H. Reme, and P. Daly (2007), Ion multi-nose structures observed by Cluster in the inner magnetosphere, *Ann. Geophys.*, *25*, 1, doi:10.5194/angeo-25-171-2007.

Weimer, D. R. (1996), A flexible, IMF dependent model of high-latitude electric potentials having "space weather"' applications, *Geophys. Res. Lett.*, *23*(18), 2549–2552, doi:10.1029/96GL02255.

Weimer, D. R., and J. H. King (2008), Improved calculations of interplanetary magnetic field phase front angles and propagation time delays, *J. Geophys. Res.*, *113*, A01105, doi:10.1029/2007JA012452.

Weimer, D. R., D. M. Ober, N. C. Maynard, M. R. Collier, D. J. McComas, N. F. Ness, C. W. Smith, and J. Watermann (2003), Predicting interplanetary magnetic field (IMF) propagation delay times using the minimum variance technique, *J. Geophys. Res.*, *108*(A1), 1026, doi:10.1029/2002JA009405.

Yamauchi, M., et al. (2006), Source location of the wedge-like dispersed ring current in the morning sector during a substorm, *J. Geophys. Res.*, *111*, A11S09, doi:10.1029/2006JA011621.

Yang, J., R. A. Wolf, F. R. Toffoletto, S. Sazykin, and C. P. Wang (2014), RCM-E simulation of bimodal transport in the plasma sheet, *Geophys. Res. Lett.*, *41*, 1817–1822, doi:10.1002/2014GL059400.

Zhang, J.-C., M. W. Liemohn, J. U. Kozyra, B. J. Lynch, and T. H. Zurbuchen (2004), A statistical study of the geoeffectiveness of magnetic clouds during high solar activity years, *J. Geophys. Res.*, *109*, A09101, doi:10.1029/2004JA010410.

Zhang, J.-C., R. A. Wolf, S. Sazykin, and F. R. Toffoletto (2008), Injection of a bubble into the inner magnetosphere, *Geophys. Res. Lett.*, *35*, L02110, doi:10.1029/2007GL032048.

Zhang, J.-C., R. A. Wolf, R. W. Spiro, G. M. Erickson, S. Sazykin, F. R. Toffoletto, and J. Yang (2009), Rice Convection Model simulation of the substorm-associated injection of an observed plasma bubble into the inner magnetosphere: 2. Simulation results, *J. Geophys. Res.*, *114*, A08219, doi:10.1029/2009JA014131.